LONG WAVELENGTH SATELLITE TOPOGRAPHY FROM LIMB PROFILES: GEOPHYSICAL IMPLICATIONS.
F. Nimmo, R.A. Parsons, *Dept. Earth & Planetary Sciences, U.C. Santa Cruz, Santa Cruz CA 95064 (fnimmo@es.ucsc.edu, rparsons@es.ucsc.edu)*, P.C. Thomas, *Dept. Astronomy, Cornell University, Ithaca, NY Cornell (pct2@cornell.edu)*, B.G. Bills, *Jet Propulsion Laboratory, Pasadena CA 91109 (bruce.bills@jpl.nasa.gov)*.

Summary We have used limb profile to derive the long-wavelength topography and variation in roughness with wavelength for the inner Saturnian satellites. Comparisons with stereo-derived topography show strong similarities between the two data sets. Most satellites show a reduction in variance (roughness) at long wavelengths, perhaps due to a transition from elastic support (at short wavelengths) to isostatic support (long wavelengths). Alternatively, the variance spectrum may be controlled by crater topography.

Introduction Limb profile may be used to determine a satellite's long wavelength topography [1], and how its roughness varies with wavelength i.e. its variance spectrum [2]. Long wavelength topography can arise from convection, compositional contrasts or shell thickness variations [3], and can affect the gravity fiel of a satellite [4]. Here we investigate both the spatial pattern and frequency behaviour of satellite limb-profil topography.

Method The limb profile are derived using the methods of [1]. Although limb profile tend to be biased high (because hills mask valleys), this effect does not appear to be significan [2]. Spherical harmonic expansions of the topography are obtained by solving the following matrix equation:

$$\underline{\hat{x}} = \left[\underline{A}^T \cdot \underline{A} + rN\underline{B}\right]^{-1} \cdot \underline{A}^T \cdot \underline{z} \qquad (1)$$

where $\underline{\hat{x}}$ contains the spherical harmonic coefficient to be determined, $\underline{A}$ depends on the location of the limb profil points, N is the number of points, $\underline{z}$ contains the topography at each point, $\underline{B}$ is an *a priori* constraint applied to regularize the solution and r is a dimensionless parameter which varies the strength of the *a priori* constraint. The specifi constraint that we adopt is that the power spectral slope is fla at long wavelengths [2].

Reducing the strength of the *a priori* constraint or increasing the maximum degree of the spherical harmonic expansion l_{max} increases the amplitude of the derived topography in areas not constrained by observations. Values of l_{max} and r were derived by comparing our model a,b and c axes with those of the ellipsoids derived by [1].

Results - Topography

Fig. 1 shows example long-wavelength topography for Enceladus, with the degree-2 tidal and rotational effects removed. The basin locations are broadly consistent with those identifie by [5] using regional stereo data. The south polar topographic low is clearly evident. Preliminary indications suggest that the topography correlates quite well with the low-order geoid [6].

Results - Roughness and Variance

Table 1 gives the global topographic variance σ^2 and also the variance at a particular wavelength k. In general these two values are correlated; the one exception is Mimas, which is rough at short wavelengths, but has a lower than expected global variance. As expected, Enceladus is smoothest by both measures. The stresses implied by the global variance ($\sim \rho g \sigma$) range from 40 kPa for Mimas to 300 kPa for Rhea, similar to present-day diurnal tidal stresses at Enceladus and Europa.

Fig. 2 plots the variance as a function of wavenumber. At short wavelengths, all bodies show a roughly -2 slope. At longer wavelengths, all bodies except Enceladus show a departure from this -2 slope i.e. there is less power than expected at long wavelengths. This transition was previously interpreted by [2] as a sign of the transition from elastic support (short wavelengths) to isostatic support (long wavelengths).

Fig. 3a plots the variance spectra relative to a line with a slope of -2. This makes deviations from a -2 slope easier to see. The approximate wavelengths at which this deviation occurs are 10 km for Enceladus, 20 km for Mimas, 100 km for Tethys, 300 km for Rhea and hard to establish for Dione. These values imply corresponding elastic thicknesses $T_e \approx 1.5$ km, 3 km, 5 km and 10 km, respectively. For Enceladus, the value obtained is somewhat larger than the 0.3 km obtained by [7] via fl xural measurements, but comparable to the range of 0.4-1.4 km found by [8] from modelling of unstable extension. For Tethys, the elastic thickness established here is similar to the range of 4.7-7.2 km obtained by [9] from fl xural profiles

An alternative possibility (except for Enceladus) is that the topography is primarily controlled by impact craters. In this case, the topographic variance will depend on the size-frequency distribution of craters [10]. To test this possibility, in Fig. 3 we plot the deviation of the topographic variance spectrum from a line with slope -2, and compare this with a similar plot ("R-plot") of crater density as a function of diameter [11]. There are some similarities between the two plots. Mimas is both the roughest and the most heavily cratered body; furthermore, both variance and crater density show a peak at intermediate wavelengths. Rhea too has very similar characteristics in both plots, except that the upturn in crater density at the longest wavelengths is not seen in the variance. Although Dione is nearly as heavily cratered as Mimas, it shows much less topographic variance. Conversely, Tethys is more lightly cratered, but shows greater roughness, perhaps as a result of its more obvious tectonic activity.

References

[1] Thomas, P.C., Icarus 208, 395-401, 2010. [2] Nimmo, F. et al., JGR 115, E10008, 2010. [3] Nimmo, F., B.G. Bills, Icarus 208, 896-904, 2010. [4] Nimmo, F., I. Matsuyama, GRL 34, L19203, 2007. [5] Schenk, P., W.B. McKinnon, GRL 36, L16202, 2009. [6] Iess, L. et al., Fall AGU P23C-02, 2010. [7] Giese, B. et al., GRL 35, L24204, 2008. [8] Bland, M.T. et al., Icarus 192, 92-105, 2007. [9] Giese, B. et al., GRL 34, L21203, 2007. [10] Rosenburg, M.A. et al., Fall AGU P42A-03, 2010. [11] Kirchoff, M.R., P. Schenk, Icarus 206, 485-497, 2010.

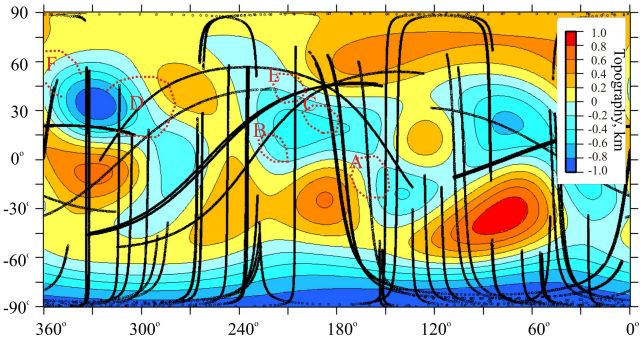

Figure 1: Enceladus topography from limb profiles plotted from $l = 3$ to $l = 6$, based on an expansion with $l_{max} = 8$ and $r = 10^4$ (see text). Contour interval is 200 m; circles are locations of limb profiles Dashed red lines and letters give approximate basin locations from stereo topography [5].

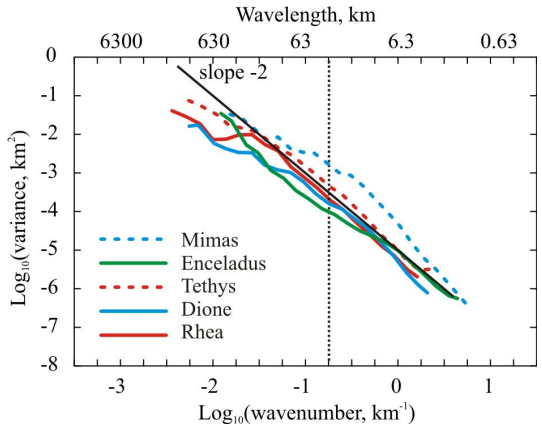

Figure 2: Topographic variance spectra for inner Saturnian satellites. Dashed vertical line indicates wavelength at which variance is tabulated in Table 1.

Body	R (km)	N	σ^2 (km^2)	Log$_{10}$ σ_k^2
Enceladus	252.1	25,750	0.20	-4.0
Dione	561.4	32,433	0.35	-3.8
Rhea	764.0	34,556	1.11	-3.7
Tethys	531.0	19,767	1.42	-3.4
Mimas	198.4	20,774	0.43	-2.8

Table 1: R is the satellite radius, N the number of limb profil points used, σ^2 is the global variance (relative to the best-fi ellipsoid of [1]) and σ_k^2 is the variance at k=0.18 km^{-1} (35 km wavelength)(see Fig. 2).

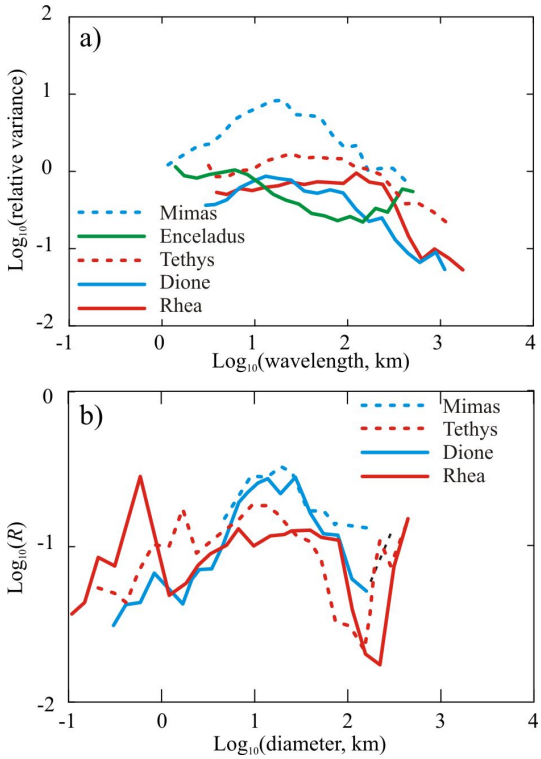

Figure 3: a) Variance from Fig 2, relative to a line with slope -2 and a variance of 10^{-3} km^2 at $k = 10^{-1}$ km^{-1}. Note that the horizontal axis is now wavelength, not wavenumber. This plot makes subtle changes in variance easier to see. b) Crater density (expressed as an R-plot, which also accentuates subtle variations) as a function of crater diameter, from [11]. This plot shows some similarities to a).